AAS 17-597

DYNAMICAL STRUCTURES IN A COMBINED LOW-THRUST MULTI-BODY ENVIRONMENT

Andrew D. Cox*, Kathleen C. Howell† and David C. Folta‡

Low-thrust trajectory design is challenging as the spacecraft position, velocity, and control histories must be specified simultaneously. Traditional approaches typically generate a single trajectory and control law via optimization algorithms. However, such solutions generally depend strongly on a feasible design that is input to the optimization process. Rather than seeking an optimal control law for each specific design problem, the focus of this investigation is additional insight from the exploration of a combined low-thrust multi-body dynamics model to guide the preliminary design process. Characteristics of key dynamical structures such as equilibrium points, periodic solutions, and manifold arcs are identified and compared to the well-understood circular restricted 3-body problem dynamics.

BACKGROUND

One of the key challenges in low-thrust trajectory design is generating a preliminary solution that simultaneously specifies spacecraft position, velocity, and thrust control histories. Although many methods exist to construct spacecraft position and velocity histories under the natural dynamics, fewer resources are available to identify thrust control strategies. Those resources that do exist often rely on optimization algorithms to solve boundary value or initial value problems that include the control variables. For example, predictor-corrector shooting algorithms have been applied to generate control histories on short low-thrust transfers between periodic orbits in the circular restricted 3-body problem (CR3BP).[1,2] A more general exploration of a low-thrust force applied to natural manifold arcs yields "attainable regions" with control histories obtained via optimization processes.[3] Similarly, collocation and direct transcription, combined with indirect optimization, have been applied to yield non-intuitive orbit geometries by leveraging a low-thrust acceleration.[4] All of these techniques employ algorithms to assign or solve for the thrust parameters. The converged solutions are, thus, often strongly dependent on the initial guess leveraged by the algorithms. Accordingly, the solution space is narrowly defined around the initial solution and a general description of nearby solutions is not typically available.

Rather than rely solely on numerical targeting and optimization algorithms to develop a low-thrust control history, the focus of this investigation is the exploration of a multi-body dynamics model that incorporates a low-thrust term; the goal is a more general set of heuristics and properties that may be applied to construct preliminary solutions. Because the addition of the low-thrust term results in a nonautonomous system, many traditional dynamical systems tools cease to apply.

*Ph.D. Student, School of Aeronautics and Astronautics, Purdue University, West Lafayette, IN 47907; cox50@purdue.edu
†Hsu Lo Distinguished Professor of Aeronautics and Astronautics, School of Aeronautics and Astronautics, Purdue University, West Lafayette, IN 47907; howell@purdue.edu
‡Senior Fellow, NASA Goddard Space Flight Center, Greenbelt, MD, 20771; david.c.folta@nasa.gov

However, by leveraging several dimension reductions, useful dynamical insights are still available. Equipped with such insights, a mission design analyst is afforded a much larger array of design options. Subsequently, optimal low-thrust trajectories that depend strongly on an initial design may be tailored more specifically to a particular mission.

As a first step toward a greater understanding of the combined low-thrust and multi-body dynamics, this investigation explores key dynamical structures. The CR3BP dynamics are augmented with low-thrust terms and dimension reductions are applied to yield a simple system capable of approximating the complex dynamics of a full-fidelity model. Next, equilibrium solutions of the low-thrust CR3BP (CR3BP-LT) equations are identified and characterized. Families of periodic orbits in the vicinity of the equilibrium points are identified and briefly explored to further understand the system dynamics. Finally, manifold arcs from the CR3BP are compared to similar motion in the CR3BP-LT model. A brief discussion of numerical (i.e., computational) considerations key to the analyses concludes the paper.

DYNAMICAL SYSTEMS FORMULATION

To begin the investigation of the combined low-thrust and multi-body dynamics, an appropriate dynamical system is formulated. The model is built on the familiar CR3BP dynamics, thus, a brief review of the CR3BP dynamics such as the Jacobi constant, periodic solutions, and invariant manifolds is supplied. The combined dynamics model, the CR3BP-LT, is constructed by augmenting the natural CR3BP equations of motion with a low-thrust term. This transformation yields a high-dimension problem that encapsulates the design difficulties common to low-thrust trajectory design. To mitigate these difficulties, dimension reduction techniques are applied to lower the problem complexity and enable an exploratory study.

Circular Restricted 3-Body Problem

The CR3BP describes the motion of a relatively small body, such as a spacecraft, in the presence of two larger gravitational point masses (P_1 and P_2) which proceed on circular orbits about their mutual barycenter (B). To simplify the governing equations and enable simple visualization of periodic solutions, the motion of the spacecraft is described in a frame ($\hat{x}\hat{y}\hat{z}$) that rotates with the two primaries, as in Figure 1. The $\hat{x}$-axis points from the larger primary to the smaller primary,

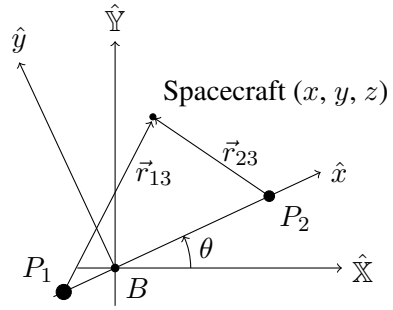

Figure 1. CR3BP System Configuration

$\hat{z}$ is parallel to the primary orbit angular momentum vector, and $\hat{y}$ completes the orthonormal set. By convention, coordinates in this reference frame are nondimensionalized such that the distance between P_1 and P_2, l_*, and angular velocity, $\dot{\theta}$, are unity.[5] Mass values are nondimensionalized

by the total system mass such that the masses of P_1 and P_2 are equal to $1-\mu$ and μ, respectively. Employing these coordinates, the position of the spacecraft, represented by (x, y, z) in the rotating frame, is described by the following equations of motion:

$$\ddot{x} - 2\dot{y} = \frac{\partial U}{\partial x}\,, \qquad \ddot{y} + 2\dot{x} = \frac{\partial U}{\partial y}\,, \qquad \ddot{z} = \frac{\partial U}{\partial z}\,, \tag{1}$$

where U is the *pseudo-potential*,

$$U = \frac{1}{2}(x^2 + y^2) + \frac{1-\mu}{r_{13}} + \frac{\mu}{r_{23}}\,, \tag{2}$$

and r_{13} and r_{23} represent the distances between the two primaries and the body of interest,

$$r_{13} = \sqrt{(x+\mu)^2 + y^2 + z^2}, \qquad r_{23} = \sqrt{(x-1+\mu)^2 + y^2 + z^2}\,. \tag{3}$$

Because the primaries are fixed in the rotating frame, these equations of motion admit a constant energy-like integral termed the *Jacobi Constant*,

$$C = 2U - v^2\,, \tag{4}$$

where v is the spacecraft velocity, $v = \sqrt{\dot{x}^2 + \dot{y}^2 + \dot{z}^2}$, relative to the rotating frame. This constant is employed to characterize motion in the CR3BP and offers a basic comparator between solutions. Note that energy and Jacobi Constant value are inversely proportional, i.e., a CR3BP trajectory with $C = 2$ is more energetic than a path with $C = 3$.

A study of the motion in the CR3BP typically begins with the identification of equilibrium solutions. The CR3BP admits five equilibrium points, also termed *Lagrange points* or *libration points*. Three of these solutions, L_1, L_2, and L_3, lie on the $\hat{x}$-axis and are known as the *collinear points*; the remaining two solutions, L_4 and L_5, are located at the vertices of equilateral triangles, equidistant from P_1 and P_2, and are named *triangular points*.[5] Periodic and quasi-periodic solutions exist within the center subspace of each libration point; these solutions include the well-known Lyapunov, halo, and vertical (i.e., vertical Lyapunov) orbit families. Such periodic orbits have been leveraged for missions including Genesis, Advanced Composition Explorer (ACE), Solar Heliospheric Observatory (SOHO), and Global Geospace Science WIND, among others.[6,7]

Of perhaps even greater interest are the stable and unstable invariant manifolds associated with many periodic solutions in the CR3BP. These manifolds guide the natural flow throughout the system, and asymptotically approach and depart from periodic solutions. Accordingly, low-cost or free transfers between various regions of the multi-body system may be achieved by leveraging manifold motion.[8–10]

CR3BP and Low-Thrust

The addition of low-thrust into the CR3BP introduces three additional state variables. Two of these states describe the thrust vector orientation and the third represents the thrust magnitude. Let the acceleration due to the low-thrust force be represented by $\vec{a}_{lt}$,

$$\vec{a}_{lt} = \frac{f}{m}\hat{u}\,, \tag{5}$$

where f is the nondimensional thrust magnitude, m is the nondimensional spacecraft mass, and $\hat{u}$ is a unit vector that orients the low-thrust acceleration. The thrust magnitude is nondimensionalized

by the CR3BP characteristic time, t_*, and characteristic length, l_*, as well as by the spacecraft reference mass, $M_{3,0}$, via the relationship

$$f = \frac{Ft_*^2}{1000 l_* M_{3,0}} \,. \tag{6}$$

In this expression, F represents the thrust magnitude in Newtons, l_* represents the distance between P_1 and P_2 in kilometers, t_* is the inverted system mean motion, $t_* = 1/n$, in seconds, and $M_{3,0}$ is the initial (wet) mass of the spacecraft in kilograms. The nondimensional mass quantity, m, represents the mass fraction of the spacecraft, $m = M_3/M_{3,0}$.

Accordingly, the augmented low-thrust CR3BP (CR3BP-LT) equations of motion are

$$\ddot{x} - 2\dot{y} = \frac{\partial U}{\partial x} + \frac{f}{m} u_x \,, \qquad \ddot{y} - 2\dot{x} = \frac{\partial U}{\partial y} + \frac{f}{m} u_y \,, \qquad \ddot{z} = \frac{\partial U}{\partial z} + \frac{f}{m} u_z \,, \tag{7}$$

where u_x, u_y, and u_z are the Cartesian components of $\hat{u}$. An additional equation governs the mass of P_3,

$$\dot{m} = \frac{-Ft_*^2}{1000 I_{sp} g_0 M_{3,0}} \,, \tag{8}$$

where I_{sp} is the constant specific impulse measured in seconds, and g_0 is the Earth standard gravity value, $g_0 = 9.8065$e-3 km/s^2. Due to the addition of this mass time-rate-of-change, the system is nonautonomous, unlike the CR3BP. Many useful dynamical systems tools do not apply to nonautonomous systems. For example, the Jacobi Constant integral is not constant in the general CR3BP-LT problem. However, a few equation manipulations and reasonable assumptions in the following sections enable the usage of some of the tools.

For the duration of this study, the thrust magnitude, f, is leveraged to describe results. To gain a level of intuition about the magnitude of f, consider the selection of spacecraft parameters listed in Table 1. The thrust values represent the maximum thrust capability of each spacecraft and the

Table 1. Low-Thrust System Comparison

Spacecraft	$M_{0,3}$ kg	F mN	a_{lt} m/s^2	f (Earth-Moon) nondim	f (Sun-Earth) nondim
Deep Space 1[11]	486	92.0	1.893e-4	6.95e-2	3.19e-2
Hayabusa[12]	510	24.0	4.706e-5	1.73e-2	0.79e-2
Dawn[13]	1218	92.7	7.611e-5	2.79e-2	1.28e-2
Lunar IceCube[14]	14	1.0	7.143e-5	2.62e-2	1.20e-2

mass values represent the launch mass (including propellant). Accordingly, the associated acceleration magnitude is near the maximum value, though the acceleration will increase if the thrust is maintained at the maximum value and the spacecraft mass decreases. The value of f is system dependent as Equation (6) includes the characteristic length and time values. This brief survey indicates that current technology leverages thrust values in the neighborhood of f = 1e-2. In the interest of demonstrating realistic scenarios, this magnitude will be utilized in the results that follow as much as is practical.

Dimension Reductions

To mitigate the increased complexity of the CR3BP-LT system, several dimension reductions are applied. A single state vector in the full spatial problem includes three position states, three velocity states, a mass state, and three thrust states for a total of 10 independent variables. First, consider simplifying the motion to be planar; this reduces the state dimension from ten to seven. Second, let the thrust magnitude be constant to eliminate another variable. With these simplifications, the low thrust acceleration may be represented as

$$\vec{a}_{lt} = \frac{f}{m}\left\{\cos\alpha \quad \sin\alpha \quad 0\right\}^T , \tag{9}$$

where α is the angle between the thrust vector and the $\hat{x}$-axis. Although the size of the state vector has been decreased, the design space remains six-dimensional (x, y, $\dot{x}$, $\dot{y}$, m, α). Further reductions are required to simplify the problem to a more manageable set of variables.

In the interest of further dimension reductions it is useful to seek a thrust pointing direction that maintains the Jacobi integral, if possible. To investigate this possibility, consider the time derivative of the Jacobi Constant in the planar problem,

$$\begin{aligned} C = 2U - v^2 &= \frac{2(1-\mu)}{r_{13}} + \frac{2\mu}{r_{23}} + x^2 + y^2 - \dot{x}^2 - \dot{y}^2 \,, \\ \frac{\partial C}{\partial \tau} &= 2\dot{x}(U_x - \ddot{x}) + 2\dot{y}(U_y - \ddot{y}) \,, \end{aligned} \tag{10}$$

where U_x is the partial derivative of U with respect to x, etc. and τ is nondimensional time. By substituting the low-thrust equations of motion (7) into Equation (10), the time derivative is rewritten as

$$\frac{\partial C}{\partial \tau} = -2\dot{x}(2\dot{y} + a_{lt,x}) + 2\dot{y}(2\dot{x} - a_{lt,y}) = -2\vec{v} \bullet \vec{a}_{lt} \,. \tag{11}$$

This equation reveals that the change in Jacobi Constant is proportional to the dot product between the rotating velocity vector and the low-thrust acceleration vector. Thus, discarding the trivial solutions, the Jacobi Constant is preserved when $\vec{a}_{lt}$ is orthogonal to $\vec{v}$. Similarly, the three-body energy is increased most quickly when $\vec{a}_{lt}$ is aligned with $\vec{v}$ and is decreased most quickly when $\vec{a}_{lt}$ is aligned with $-\vec{v}$. Accordingly, in the planar problem the Jacobi-preserving thrust pointing is described by

$$\hat{u} = \frac{\pm 1}{\sqrt{\dot{x}^2 + \dot{y}^2}}\left\{-\dot{y} \quad \dot{x}\right\}^T . \tag{12}$$

For easy referencing, let the positive case be *left-pointing* (i.e., $\hat{u}$ points left from $\vec{v}$) and the negative case be *right-pointing*.

Return now to the dimension reduction discussion. With the planar, constant thrust assumption the problem dimension is reduced from ten to six. By defining the thrust pointing vector, $\hat{u}$, as a function of the velocity states in a way that preserves the CR3BP Jacobi integral, the dimension is further reduced to four. Finally, Poincaré mapping techniques resolve the design space to three dimensions, a more manageable set.

EQUILIBRIUM SOLUTIONS

The first step in describing the CR3BP-LT dynamics is determining and characterizing the equilibrium solutions. To do so, consider the CR3BP-LT equations of motion in Equation (7), simplified

as described above but with an arbitrary thrust pointing direction in the plane, as in Equation (9). Assume for the time being that the mass time-rate-of-change, $\dot{m}$, is zero but thrust, f, is nonzero. Equilibrium solutions of this system satisfy the equations

$$\frac{\partial U}{\partial x} + \frac{f}{m}\cos\alpha = 0\,, \qquad \frac{\partial U}{\partial y} + \frac{f}{m}\sin\alpha = 0\,. \tag{13}$$

Because U is a nonlinear function of x and y, no analytical solution is apparent and equilibria are located via a multidimensional Newton-Raphson process. Clearly, the solution is a function of both the position states x and y, but also of the thrust, mass, and thrust pointing angle. Consider a case with $m = 1$ for simplicity and values of f ranging from 3.00e-3, a small magnitude, to 5.00e-1, a large magnitude. The Newton-Raphson process yields a continuum of solutions for $\alpha \in [0\, 2\pi]$, plotted in Figure 2. When the thrust magnitude is low, at $f = 3.00\text{e-}3$, the CR3BP-LT equilibrium

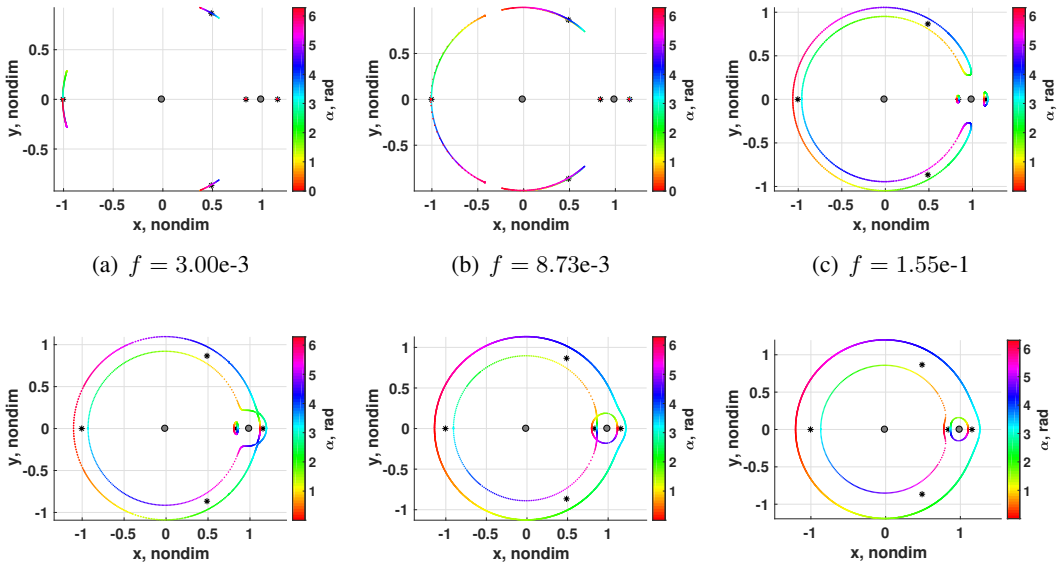

(a) $f = 3.00\text{e-}3$ (b) $f = 8.73\text{e-}3$ (c) $f = 1.55\text{e-}1$

(d) $f = 2.60\text{e-}1$ (e) $f = 3.50\text{e-}1$ (f) $f = 5.00\text{e-}1$

Figure 2. Evolution of the CR3BP-LT equilibrium solutions over a range of thrust magnitudes, plotted as colored points over $\alpha \in [0,\, 2\pi]$. The CR3BP Lagrange points are plotted as black asterisks for reference, and the Earth and Moon are located by grey circles.

solutions remain near the natural CR3BP solutions, librating as α varies. When $\alpha = 0$ or π, the collinear equilibrium solutions remain collinear, i.e., at $y = 0$. However, as the thrust pointing vector rotates away from the $\pm\hat{x}$ orientations, the solutions move further from the natural solution. Similarly, the CR3BP-LT equilibrium near L_4 is closest the natural solution when $\alpha = \pi/3$ and $\alpha = -2\pi/3$, and the perturbed L_5 point is closest to the natural solution when $\alpha = -\pi/3$ and $\alpha = 2\pi/3$.

It is clear that the magnitude of the location difference between the CR3BP-LT equilibria and CR3BP equilibria is proportional to f. For example, the oscillations of the L_3, L_4, and L_5 points are noticeably larger in Figure 2(b), with $f = 8.73\text{e-}3$, compared to Figure 2(a), with $f = 3.00\text{e-}3$. However, as the thrust magnitude increases further, the structure of the solutions change: The L_4 and L_5 solutions merge with the L_3 solution to form a C-shaped contour, as in Figure 2(c).

This contour still includes several solutions for most α values, as depicted by the repeated colors at different locations. As f continues to grow, this $L_{3,4,5}$ structure merges with the L_2 structure (Figure 2(d)) and then with the L_1 structure (Figure 2(e) until, at large values of f, the continuum of equilibria forms a shape similar to the planar zero velocity contour in the CR3BP (Figure 2(f)). In this case, however, the contour represents both zero velocity and zero acceleration. Note that each point on this "zero acceleration contour" (ZAC) exists at a single instantaneous α value and, thus, is not a general boundary on motion like the zero velocity contours are in the CR3BP.

The locations of the CR3BP-LT equilibria and the angles associated with each point along the structures are available from an analysis of the natural CR3BP rotating acceleration vector. Consider the process in reverse order: choose a point, then determine the magnitude and angle of the low-thrust vector that will sum with the natural acceleration vector to yield zero acceleration at that point. For example, a CR3BP-LT equilibria at $x = y = 0.5$ exists when $f \approx$ 1e0, the same magnitude as the natural acceleration depicted in Figure 3(a). The thrust angle associated with this

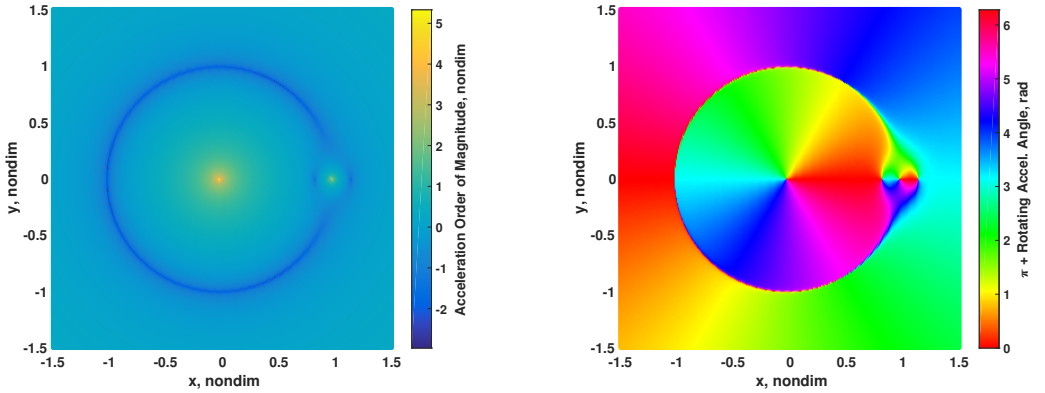

(a) Acceleration Magnitude

(b) Acceleration Angle, Rotated By π Radians

Figure 3. Characteristics of the natural rotating acceleration field in the Earth-Moon CR3BP

point is "chosen" to be opposite the direction of the natural acceleration vector at the same location. Accordingly, at (0.5, 0.5), the low-thrust equilibrium is characterized by the opposing angle, $\alpha \approx 1$ radian, as depicted by the map of natural acceleration angles (rotated by π radians) in Figure 3(b).

A comparison of the maps in Figure 3 with the ZAC structures in Figure 2 further supports this link. Each ZAC traces out a curve of constant acceleration magnitude in Figure 3(a) and each point on the contour is characterized by the angle depicted at the same (x, y) coordinate in Figure 3(b). Accordingly, a full representation of these zero acceleration contours in the CR3BP-LT is available from the natural dynamics of the natural CR3BP. The implications of the shifting equilibria for trajectory design remain an area of future work. Farrés and Miguel perform a similar analysis on the dynamics of a solar sail in the CR3BP and offer some applications for solar sailing trajectory design.[15]

The linear stability of the equilibria along the contours offers additional insight as the stability offers a general description of the local dynamical structure. Such a linearization is available from a first-order Taylor series expansion around each of the solutions. Let $\vec{q} = \begin{Bmatrix} x & y & \dot{x} & \dot{y} \end{Bmatrix}$ be the state vector and $\dot{\vec{q}} = \begin{Bmatrix} \dot{x} & \dot{y} & \ddot{x} & \ddot{y} \end{Bmatrix}$ describe the equations of motion. The linearized dynamics

about some solution, $\vec{q}_e$, are described by

$$\delta\dot{\vec{q}}_e = \frac{\partial\dot{\vec{q}}}{\partial\vec{q}}\Big|_{\vec{q}_e} \delta\vec{q}_e \,, \tag{14}$$

where the matrix of partial derivatives is given by

$$\frac{\partial\dot{\vec{q}}}{\partial\vec{q}}\Big|_{\vec{q}_e} = \boldsymbol{A} = \begin{bmatrix} 0 & 0 & 1 & 0 \\ 0 & 0 & 0 & 1 \\ U_{xx} & U_{xy} & 0 & 2 \\ U_{xy} & U_{yy} & -2 & 0 \end{bmatrix} . \tag{15}$$

In this equation, U_{xy} denotes the second partial derivative of U with respect to x and y. As with the CR3BP, the order of the differentiation does not change the value of the partial derivative.

The linear dynamics described by Equation (14) are characterized by the eigenvalues of $\boldsymbol{A}$. Thus, a solution to (14) is composed of up to four modes, each associated with one of the eigenvalues. An eigenvalue with negative real part indicates asymptotic stability about the origin, while an eigenvalue with positive real part indicates instability, i.e., an exponential departure from the origin. Eigenvalues with zero real part are termed *center* eigenvalues and represent oscillatory modes that neither approach nor depart the equilibrium point. Finally, eigenvalues with nonzero real and imaginary parts are termed *spiral* modes and combine oscillatory motion with convergent or divergent behavior. Because the system is Hamiltonian when mass, thrust, and α are constant, these eigenvalues occur in pairs: real eigenvalues form a *saddle* structure with $\pm\lambda$, while center and spiral eigenvalues occur in complex conjugate pairs, λ and $\bar{\lambda}$.

To compare the stability of the CR3BP-LT equilibrium solutions with the natural CR3BP solutions, the eigenvalues of the $\boldsymbol{A}$ matrix are computed for each point along the ZAC. The local dynamics about each point are split into three categories based on the type of eigenvalue pairs: *saddle* $\times$ *center*, *center* $\times$ *center*, and *spiral* $\times$ *spiral*. While other pairings are possible, they do not occur in practice for the systems depicted in this investigation. The stability of the points along each ZAC from Figure 2 are depicted by colored points in Figure 4. Red points possess a *saddle* $\times$ *center* subspace, blue points possess a *center* $\times$ *center* subspace, and black points posses a *spiral* $\times$ *spiral* subspace. At low magnitudes, the linearized dynamics near the five solution structures are identical to the natural, CR3BP dynamics: the three collinear point structures are characterized by a *saddle* $\times$ *center* subspace and the triangular point structures possess a *center* $\times$ *center* subspace. At larger thrust levels, the oscillatory motion associated with the triangular points transitions to spiral behavior. However, regardless of the thrust magnitude, motion in the vicinity of the collinear points remains characterized by the pair of saddle and center modes.

Similar to the locations and angles of the CR3BP-LT equilibria, the stability characteristics of the points along the ZAC structures are available from an analysis of the natural CR3BP model. Note that the linearization, $\boldsymbol{A}$, depends only on the CR3BP pseudo-potential, U, which does not include any of the low-thrust parameters. Accordingly, the stability of the linearized dynamics over a grid of points in the plane is computed and colored consistent with the scheme employed above. The results, plotted in Figure 5, mirror the patterns observed in the contours in Figure 4. For example, consider the $L_{3,4,5}$ equilibria contour in Figure 4(c). The location of the inner portion of the contour corresponds to the red *saddle* $\times$ *center* depicted in the system map (Figure 5). Similarly, the outer portion of the contour passes through the black *spiral* $\times$ *spiral* region in the system map. A

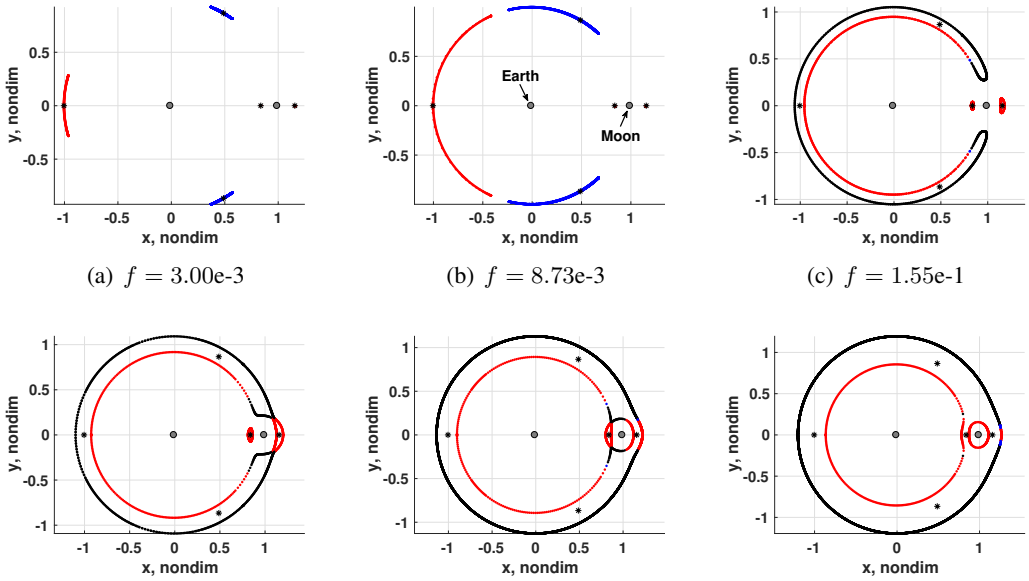

(a) $f = 3.00\text{e-}3$ (b) $f = 8.73\text{e-}3$ (c) $f = 1.55\text{e-}1$

(d) $f = 2.60\text{e-}1$ (e) $f = 3.50\text{e-}1$ (f) $f = 5.00\text{e-}1$

Figure 4. Stability characteristics of the Earth-Moon CR3BP-LT System at various thrust magnitudes. Red points indicates *saddle* $\times$ *center* motion, blue indicates *center* $\times$ *center* motion, and black indicates *spiral* $\times$ *spiral* motion.

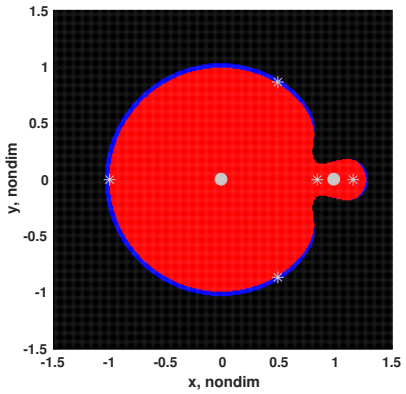

Figure 5. Stability of linearized dynamics about static planar states in the Earth-Moon CR3BP. Red points correspond to *saddle* $\times$ *center* motion, blue to *center* $\times$ *center*, and black to *spiral* $\times$ *spiral*

comparison of the other contours and the system map reveals the same patterns: the linear stability of each point on each contour is a function only of the position of the point in the rotating frame. It is clear that oscillatory motion is found throughout the system; the linear dynamics around every point includes an oscillatory or spiral subspace. While many of these oscillatory modes are coupled with diverging behavior, these results imply that periodic and quasi-periodic structures are likely possible regardless of the low-thrust acceleration magnitude. A more detailed correlation between the stability of an equilibrium and the existence of nearby structures remains an area of future study.

PERIODIC SOLUTIONS

The oscillatory modes of the linearized dynamics about the CR3BP-LT equilibrium solutions predict periodic motion in the nonlinear model. Additionally, it is expected that these periodic solutions are similar to those found in the natural CR3BP, particularly when the magnitude of the low-thrust perturbation is small. Thus, rather than initializing a family of periodic orbits from a linear approximation in the combined low-thrust CR3BP model, the natural CR3BP periodic orbits are leveraged as initial guesses for the low-thrust periodic orbits. Consistent with the dimension reductions described above, let the thrust magnitude remain constant and let the thrust direction be chosen to preserve the Jacobi constant, i.e., $\hat{u}$ is described by Equation (12). Unlike the equilibrium point analyses, mass is not assumed to be constant. Accordingly, the low-thrust orbits described in the following pages are periodic only in position and velocity, not in mass. However, note that the the mass change is relatively small and can be reasonably approximated as a constant parameter. Given these assumptions, a natural parameter continuation algorithm is employed to generate a family of periodic solutions. The resulting low-thrust Lyapunov families, plotted in Figure 6, are propagated with left-pointing thrust at a constant magnitude f = 1e-2, consistent with the capabilities of past and current low-thrust-enabled spacecraft. Note that the extents of each orbit family are limited

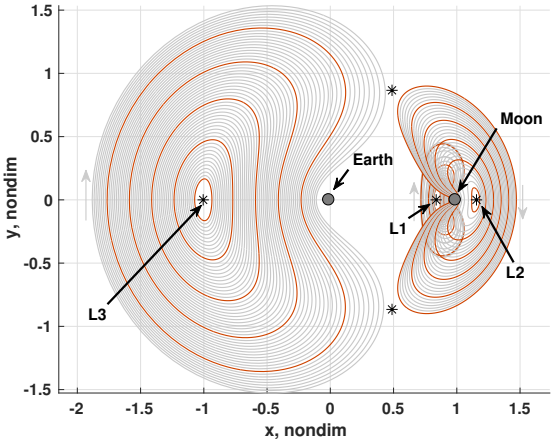

Figure 6. Lyapunov Families with left-pointing thrust, f = 1e-2, in the Earth-Moon CR3BP-LT system.

by the simple natural parameter continuation method leveraged to generate the family and are not representative of the dynamical limits of the families.

At this thrust level, these majority of the family members are visually identical to the natural CR3BP Lyapunov orbits. However, at high energy values (low Jacobi values), the differences between the low-thrust and natural solutions becomes more apparent, as illustrated in Figure 7. At moderate energy levels, e.g. $C = 2.95$ in Figure 7(a), the difference between the CR3BP (black) and CR3BP-LT (blue) periodic orbits is very small. As the energy level increases and C decreases, the differences become more pronounced. The same general pattern is observed for the other Lyapunov families.

The orbit families in Figure 6 represent one type of orbit family in the CR3BP-LT in which thrust magnitude is constant and the Jacobi value varies along the family. Consider an alternative family with a constant Jacobi value and variable thrust magnitude. Such families of L_1 and L_2 planar

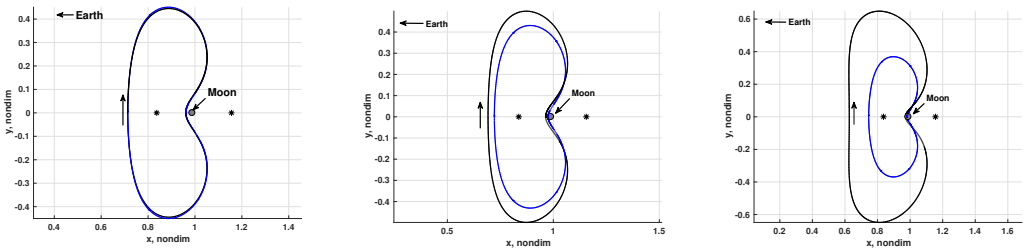

(a) $C = 2.95$ (b) $C = 2.937$ (c) $C = 2.900$

Figure 7. Earth-Moon L_1 Lyapunov orbits in the CR3BP (black) and CR3BP-LT (blue) compared over a range of energy levels. As energy increases and C decreases, the differences grow more pronounced.

.

orbits at $C = 3.10$ are depicted in Figure 8 with thrust magnitudes, depicted by color, varying from $f =$ 1e-6 to $f =$ 1e2. The family members with very small thrust magnitudes, colored dark

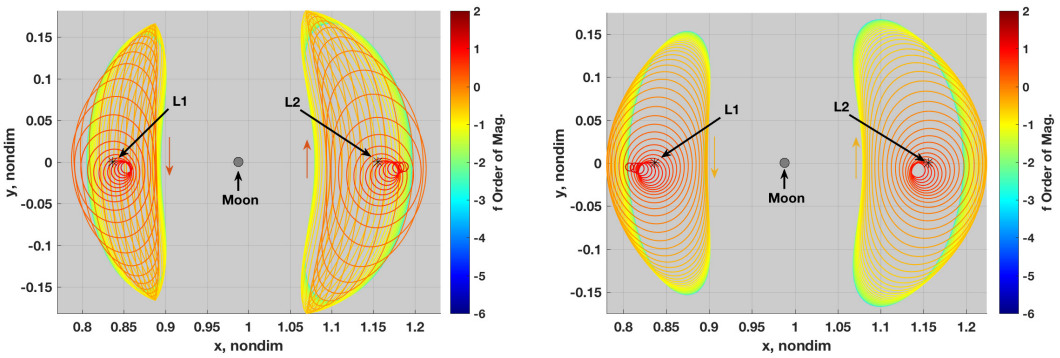

(a) Left-Pointing Thrust (b) Right-Pointing Thrust

Figure 8. Families of L_1 and L_2 Lyapunov orbits at $C = 3.10$ in the Earth-Moon system

and light blue, are visually identical to the natural CR3BP Lyapunov orbits at the prescribed Jacobi constant value. In fact, these similarities persist up to thrust magnitudes of approximately $f =$ 1e-2, consistent with the families plotted in Figure 6. As the magnitude increases, the familiar bean-shaped structures begin to change. When the thrust is left-pointing, the top and bottom edges of the structure come to a point; at different energy levels, these points can transition to loops. As the left-pointing thrust magnitude increases further, the orbits decrease in size and converge to small elliptical orbits near the natural Lagrange points. The right-pointing thrust results are similar but notably lack the transition through orbits with pointed ends. Instead, the evolution with thrust magnitude trends continuously to small elliptical orbits near the Lagrange points. While these small, nearly circular structures are interesting and illustrate the family evolution, note that the associated thrust magnitudes are impractical in a modern low-thrust system. The value $f = 10$, indicated by the red-colored orbits, is equivalent to a 13.6 Newton thrust delivered continuously by a 500 kg spacecraft in the Earth-Moon system.

Similar families of orbits are computed for $C = 3.0$ in the vicinity of the natural L_3 Lagrange point. The left-pointing and right-pointing results, plotted in Figure 9, evolve along the same thrust magnitude range as the L_1 and L_2 families. The evolution of the right-pointing family is similar

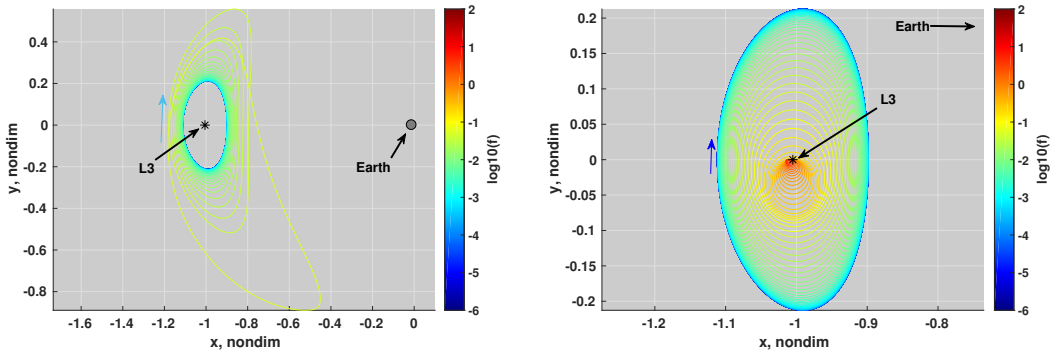

(a) Left-Pointing Thrust

(b) Right-Pointing Thrust

Figure 9. Family of L_3 Lyapunov orbits at $C = 3.00$ in the Earth-Moon system

to the low-thrust L_2 family; the size of the solutions decrease as thrust magnitude increases and converge to a small elliptical orbit near the natural L_3 point. The left-pointing results demonstrate a different evolution. Rather than shrinking, the orbits increase in size as f grows. The final converged family member is oriented differently and appears to trend toward the L_5 planar orbit families. However, experimentation with this case reveals that the evolution of the family may alternatively trend toward L_4 if the continuation process is seeded differently. A more robust continuation algorithm is required to investigate this phenomenon further. However, the general growth trend between the left- and right-pointing families is consistent. This result is not surprising when the thrust direction is considered in the context of the orbit revolution direction. All three Lyapunov families rotate in a clockwise direction, thus, a left-pointing thrust perturbs the orbit outward from the center while a right-pointing thrust perturbs the orbit inward to the center.

As a final example of a periodic orbit in the CR3BP-LT model, consider a solution converged with variable thrust pointing (i.e., not constrained to left- or right-pointing). An initial guess for such a periodic orbit, plotted in blue in Figure 10(a), is constructed by propagating a natural L_1 Lyapunov orbit with a thrust vector constrained to the right-pointing direction and a thrust magnitude of zero. Accordingly, the angle between $\vec{v}$ and $\hat{u}$ on the natural solution, ploted in blue in Figure 10(d), remains constant at -90°. The corresponding α history in Figure 10(c) evolves continuously as the velocity vector rotates along the orbit. Finally, this initial guess maintains a constant Jacobi value, as is evident in Figure 10(b).

The initial solution is passed into a differential corrector and the thrust is "turned on" to $f =$ 1e-2. Additionally, the thrust vector is not constrained but is allowed to vary bewteen segments, resulting in a turn-and-hold-like α time history. A line-search algorithm is leveraged to choose an appropriate step size in the differential corrections process and avoid stepping out of the basin of convergence.[16] The converged, periodic solution remains very similar to the natural Lyapunov orbit, as observed in the previous orbit families at this thrust magnitude. However, unlike the previous solutions, the energy fluctuates over the duration of the orbit, as plotted in red in Figure 10(b). This energy

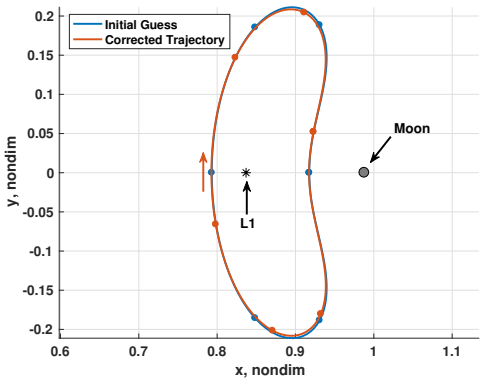

(a) Solutions in Configuration Space

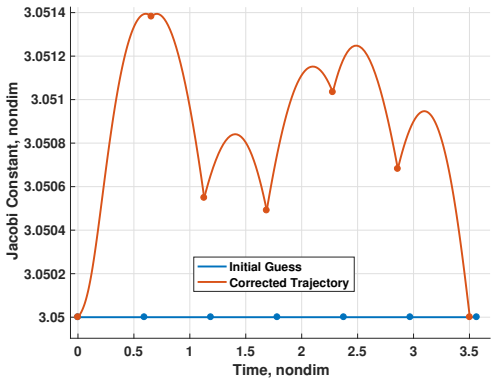

(b) Jacobi Constant Time History

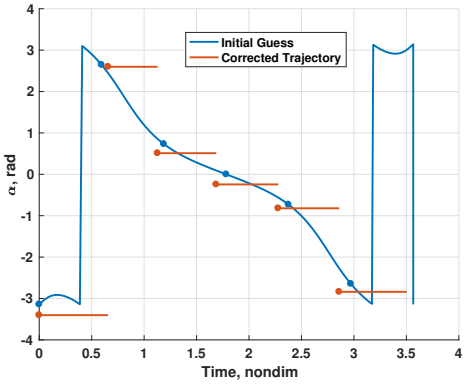

(c) Thrust Pointing Relative to $\hat{x}$

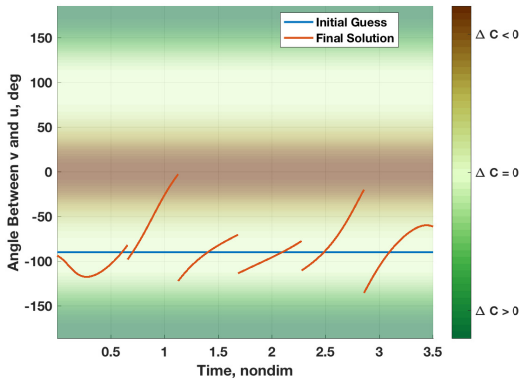

(d) Thrust Pointing Relative to $\vec{v}$

Figure 10. Comparison of Periodic L_1 Orbits. The initial guess (blue) leverages right-pointing thrust and maintains the Jacobi constant. The thrust pointing on the final solution is free to vary and the Jacobi constant varies accordingly.

fluctuation is due to the variation between the converged thrust direction and the Jacobi-preserving thrust direction of the initial guess.

Accordingly, the thrust pointing time histories are of particular interest. The relative angle between $\hat{u}$ and $\vec{v}$, depicted in Figure 10(d), remains in the vicinity of the initial guess. This phenomenon is also evident in the α time history in Figure 10(c); each segment of constant α approximates the continuous α profile of the initial guess. An additional link between the thrust pointing and energy histories is available from the contour background in Figure 10(d). As derived previously, the change in Jacobi constant, ΔC, is zero when the thrust vector is instantaneously orthogonal to the velocity vector. Accordingly, the bands at $\pm 90^\circ$ are light green to indicate $\Delta C = 0$. Similarly, when the thrust and velocity vector are aligned, energy increases or Jacobi constant decreases; this region around 0° is marked by a brown band. Finally, energy decreases (Jacobi increases) when the velocity and thrust vectors are antiparallel; these bands at $\pm 180^\circ$ are dark green. Note that this background color profile is a qualitative descriptor. The precise color shade is not associated with a specific Jacobi constant rate-of-change as this varies with thrust magnitude, velocity magnitude and direction, and position.

A comparison between the thrust pointing history (relative to the velocity vector) and the Jacobi constant history reveals a direct link. During the first trajectory segment, the thrust angle of the converged solution dips below the Jacobi-preserving angle (as in Figure 10(d)) and the corresponding segment in the Jacobi constant time history plot increases (as in Figure 10(b)). On the next segment, the thrust angle shifts to the opposite side of the Jacobi-preserving angle and the Jacobi constant trend reverses direction. Even the small dimple in the Jacobi constant at the second node is described by the difference between the thrust pointing at the end of the first segment and the beginning of the second segment. Similar analyses reveal that the entire Jacobi constant time history is linked to the thrust pointing in the same way.

This single converged solution demonstrates only one of many periodic orbits with variable thrust pointing. Initializing the corrections process with a left-pointing guess rather than the right-pointing guess leveraged above yields an entirely different orbit. These solutions, combined with the other families discussed here, establish the existence of infinitely many periodic solutions in the CR3BP-LT model. The choice of thrust magnitude, energy level, thrust pointing, and even initial guess are all important design variables when seeking a converged solution.

MANIFOLD ARCS

Another key set of structures in the three-body problem is invariant manifolds. Among the commonly used manifolds are the stable and unstable manifolds associated with periodic orbits. These structures describe the flow into and out of the periodic solutions and are frequently leveraged to construct transfers between different regions of the system. Although families of periodic orbits in the CR3BP-LT have been constructed, their manifolds remain a subject of future investigation. Instead, consider the manifolds of a natural CR3BP periodic orbit that are augmented with low-thrust. A typical mission scenario may leverage low-thrust to depart the periodic orbit on the manifold arc. Furthermore, a continued low-thrust segment while on the manifold arc may further adjust the spacecraft path toward a desired goal.

To illustrate the effects of low-thrust on manifold geometry, consider the stable and unstable manifolds of an L_1 Lyapunov orbit in the Jupiter-Europa CR3BP. Let $\boldsymbol{\phi}(T, 0)$ be the Monodromy matrix associated with the periodic orbit, and let $\boldsymbol{\phi}(\tau_i, 0)$ be the state transition matrix from the initial state on the periodic orbit to some state, $\vec{q}_i$, at some time-of-flight, τ_i, from the initial state. Finally, let $\vec{\gamma}_s$ and $\vec{\gamma}_u$ be a pair of stable and unstable eigenvectors, respectively, of the Monodromy matrix. The initial state of a stable manifold arc is, thus,

$$\vec{q}_{s,i} = \vec{q}_i \pm \epsilon \frac{\boldsymbol{\phi}(\tau_i, 0)\vec{\gamma}_s}{\left\| \boldsymbol{\phi}(\tau_i, 0)\vec{\gamma}_s \right\|}, \tag{16}$$

where ϵ is a small step-off distance chosen to expedite the evolution of the manifold arc. Initial states for unstable manifold arcs are chosen in a similar manner by leveraging the unstable eigenvector. When propagated in the natural CR3BP, these initial states yield the familiar stable and unstable manifolds of the L_1 orbit, as plotted in red and blue in Figure 11. The gray C-shaped structure represents the *forbidden region* (i.e., the *zero velocity surface*) at the chosen energy level of $C = 3.0034742$. The spacecraft is free to move in the system but cannot pass through the forbidden region. Accordingly, the manifold arcs appear to "bounce" off the grey surface in the plot. The low-thrust augmented manifold arcs begin from the same initial states as the natural manifold arcs but are propagated with low-thrust at various thrust magnitudes. In the left frame, the low-thrust propagations are conducted with left-pointing thrust. Compared to the natural manifold tubes, the

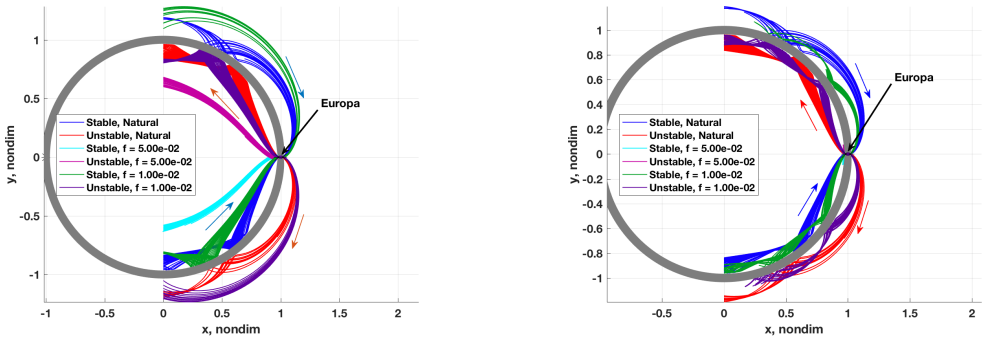

(a) Left-Pointing Augmented Manifold Arcs

(b) Right-Pointing Augmented Manifold Arcs

Figure 11. Manifold Arcs and Low-Thrust Augmented Manifold Arcs in the Jupiter-Europa System

low-thrust augmented tubes are bent in the direction of the thrust vector. This is particularly evident with the manifold tubes interior to the forbidden region. The purple and green tubes, which represent low-thrust propagations with $f =$ 1e-2, are bent further inward (toward the $\hat{x}$-axis) than the blue and red natural manifolds. The cyan and magenta tubes, propagated with $f =$ 5e-2, exhibit an even more pronounced shift. Similarly, the manifold tube geometry changes in the right frame (right-pointing thrust) reflect the thrust direction. As thrust increases, the manifold tubes are bent closer and closer to the forbidden region surface. In this representation, the augmented manifolds with $f =$ 5e-2 are effected very strongly and are only barely visible near Europa in the interior region. Accordingly, the the manifold tube geometry may be manipulated by implementing low-thrust while simultaneously preserving the Jacobi constant. This conclusion implies that low-thrust is useful to manipulate the natural structures to create "bridges" between otherwise isolated dynamical structures in the natural CR3BP.

A clear depiction of such dynamical bridges is available when Poincaré mapping techniques are applied. Consider a map of motion in the Earth-Moon CR3BP described by the surface of section,

$$\boldsymbol{\Sigma} = \left\{ x, \dot{x} \;\middle|\; y = 0,\, \dot{y} > 0,\, C = 3.15 \right\}, \tag{17}$$

plotted in Figure 12(a). The gray background represents a general puncture plot of motion in the Earth-Moon system. Each gray point represents the return of a propagated trajectory to the $y = 0$ hyperplane. Concentric rings represent quasi-periodic structures and are centered around a periodic solution, i.e., a fixed point on the map. The blue and red points mark the returns of the stable and unstable L_1 Lyapunov manifolds, respectively, to the hyperplane. In the natural CR3BP, these manifold arcs act as separatrices bewteen motion that transits in and out of the system and motion that remains bounded.[8–10, 17] This characteristic is depicted on the map as the regions within the manifold structures are largely empty of grey points; any arcs that puncture the hyperplane within the manifold structures depart and do not return to the map in a predictable manner.

When the natural Earth-Moon Poincaré map (grey) is overlaid with the low-thrust augmented manifold arc returns, opportunities to link previously separated structures become apparent. For example, consider the large island of quasi-periodic motion in the center of the map. The natural manifold arcs, plotted in Figure 12(a), bound this structure but do not provide access to it. However, when left-pointing thrust is applied, the resulting augmented manifold arcs, plotted in Figure 12(b),

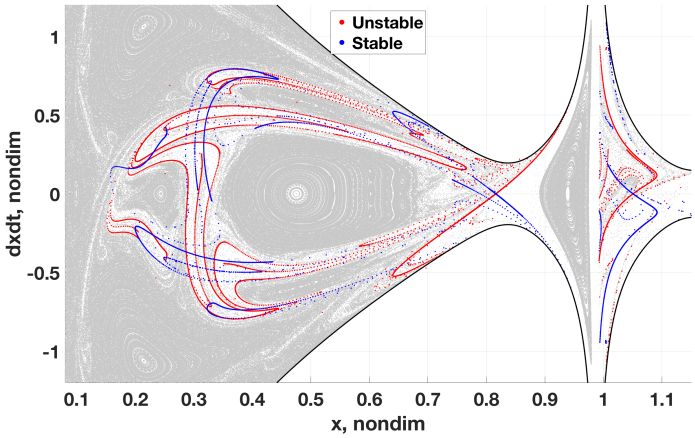

(a) Natural Manifolds

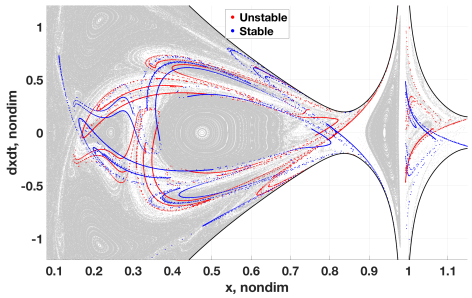

(b) Left-Pointing Thrust Augmented Manifolds at $f = 3.67\text{e-}2$

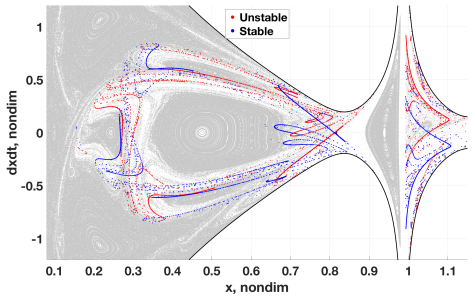

(c) Right-Pointing Thrust Augmented Manifolds at $f = 3.67\text{e-}2$

Figure 12. Poincaré maps of motion in the Earth-Moon System at $C = 3.15$. The grey background plot represents the natural motion while colored points represent returns of natural and low-thrust augmented manifolds to the map.

shift to intersect the island. Accordingly, an application of left-pointing thrust on a subset of the L_1 manifold arcs yields transfers between the unstable L_1 Lyapunov orbit and the stable center island. The right-pointing thrust augmented manifolds, illustrated in Figure 12(c), supply similar transfer opportunities. As the thrust magnitude grows, the low-thrust augmented manifolds reach larger and larger regions of the map that are inaccessible to the natural manifolds.

Due to the existence of low-thrust periodic orbits in the CR3BP-LT model, many other combinations of orbits and manifolds may be leveraged for trajectory design. As discussed above, low-thrust augmented manifolds associated with natural periodic orbits offer transit options between naturally separated dynamical structures. Similar analyses of the low-thrust manifolds associated with low-thrust periodic orbits may reveal similar design opportunities. Additionally, natural motion that asymptotically approaches and departs from the low-thrust periodic solutions is of interest. A detailed study of such manifolds remains an area of future investigation.

NUMERICAL CONSIDERATIONS

The addition of a low-thrust term to the CR3BP dynamics perturbs the natural motion in a similar manner to other natural and artificial perturbations such as celestial bodies and algorithmic numerical errors . Accordingly, a discussion of the relative magnitude of these perturbing terms is warranted. Consider first the influence of gravitational perturbations. The relative equations of motion that govern a spacecraft, P_s, relative to some primary mass, P_1, in an inertial frame are expressed by

$$\ddot{\vec{R}}_{1s} = \frac{-G(M_1 + M_s)}{R_{1s}}\vec{R}_{1s} + G\sum_{j=2}^{n} M_j \left(\frac{\vec{R}_{j1}}{R_{j1}^3} - \frac{\vec{R}_{js}}{R_{js}^3}\right), \tag{18}$$

where object j is some perturbing body. The first term on the right side of the equation is often named the *dominant* term and describes the motion of the spacecraft due to the gravitational interaction between P_1 and the spacecraft. The second term, i.e., the *perturbing term(s)*, accounts for the effect of each perturbing body on both P_1 and the spacecraft. Accordingly, the magnitude of each perturbing term in the sum supplies insight about the impact a perturbing body has on the spacecraft motion.

To determine a sense of the magnitude of several perturbing bodies on a spacecraft in the Earth-Moon system, the dominant and perturbing acceleration magnitudes are computed over a grid of points in the plane of the rotating frame. Precise ephemerides for the Earth, Moon, and perturbing bodies are obtained from the SPICE data kernels[18] for a 10-year period. The acceleration magnitude for each grid point is averaged over the 10-year data set to yield a surface of acceleration magnitudes in the system.

As an example, consider the acceleration magnitudes for a spacecraft orbiting the Earth. Accordingly, P_1 is the Earth and the relevant perturbing bodies are the Moon and Sun. To reflect the environment of the CR3BP, both the Earth dominant and Moon perturbing acceleration magnitudes are combined into a single acceleration surface in Figure 13. Note that the coordinates are con-

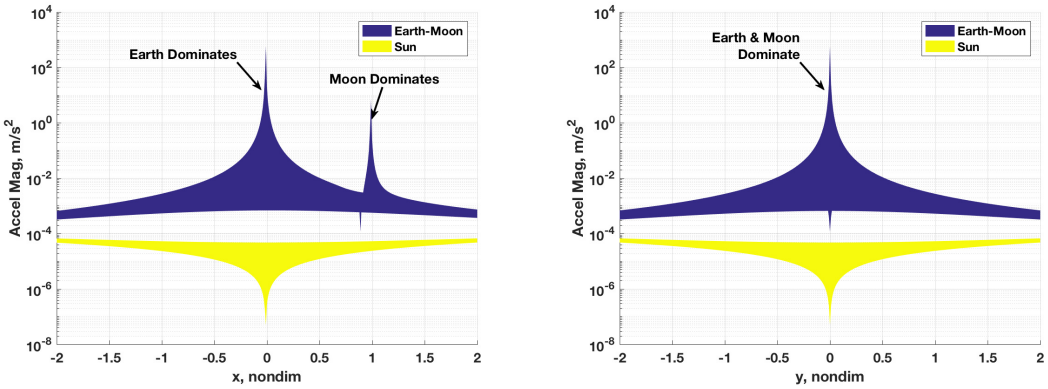

(a) xz-Projection (b) yz-Projection

Figure 13. Earth-Centered Acceleration Magnitudes

sistent with the nondimensional CR3BP rotating frame, with the Earth and Moon located on the x-axis, the Earth at $x = -\mu$ and the Moon at $x = 1 - \mu$. Although the acceleration surface is three-dimensional, the two projections in Figure 13 represent the key characteristics.

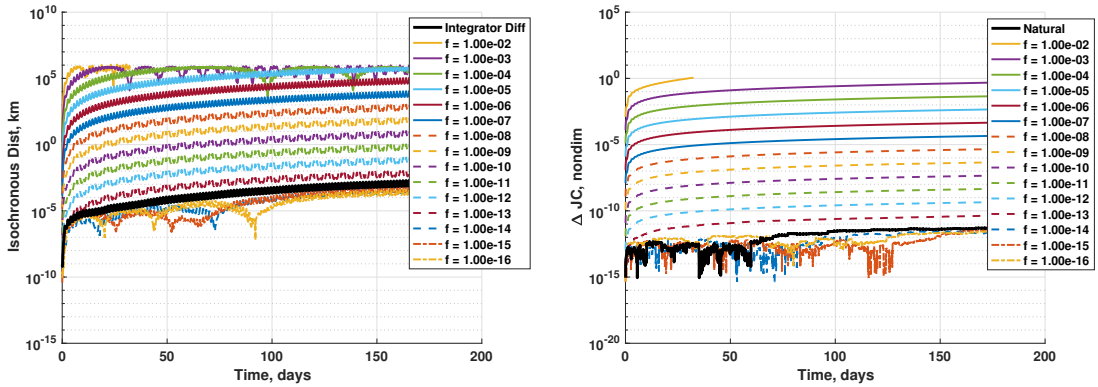

(a) Isochronous Distance Between Trajectories

(b) Change in Jacobi Constant over Time

Figure 14. Comparison of trajectories with various low-thrust acceleration magnitudes and a natural baseline solution

In addition to the Earth and Moon acceleration magnitude, the perturbing acceleration from the sun is included. The solar perturbation is smallest at points near the Earth and grows to a maximum of approximately 7e-5 m/s^2. This maximum magnitude is consistently smaller than the Earth-Moon acceleration magnitude within the typical three-body environment ($-2 < x < 2$, $-2 < y < 2$). To compare the solar perturbation to low thrust, consider the tabulated accelerations in Table 1. The acceleration magnitudes for each spacecraft are comparable to the maximum solar perturbation magnitude. Thus, it is not prudent to ignore the solar perturbation when the spacecraft is far from either primary. However, when the spacecraft is near the primaries, particularly the Earth, the magnitude of the solar perturbation decreases and the low-thrust acceleration is several times more significant than the solar term. These regions of reduced solar perturbation include the vicinities of the collinear Lagrange points and the space near the Earth and Moon. Accordingly, solar perturbations are neglected in this initial study of the combined low-thrust and multi-body dynamics.

Similar to the investigation of celestial perturbations, it is useful to determine the minimum low-thrust magnitude at which the algorithmic numerical errors are more significant than the dynamical perturbation. To investigate this phenomenon, a series of numerical integrations with decreasing thrust magnitude are compared to a baseline case in Figure 14(a). The baseline trajectory is numerically integrated for 100π nondimensional time units in the Earth-Moon CR3BP with a variable-step, variable-order, Adams-Bashform-Moulton method in both C++ (via the Gnu Science Library) and in Matlab. The propagated solutions are evaluated at equally spaced time steps and the distance between isochronous points is evaluated. The differences between these two solutions, plotted in black, are due only to differences in the integration algorithms and represent the minimum detectable perturbation. Each low-thrust arc is propagated from the same initial state as the baseline trajectories with a velocity-aligned thrust vector. When the thrust magnitude is large, the isochronous distance between the low-thrust propagation and the baseline propagations is large, as in Figure 14(a). These results show that when the thrust magnitude is at or below $f =$ 1e-14, the low-thrust perturbation is indistinquishable from the algorithmic differences.

An additional check is available by evaluating the change in Jacobi constant over each propagation. The baseline arcs are propagated without low-thrust and should have a constant Jacobi value. The only changes observed are, thus, due to numerical artifacts. Because the low-thrust vector is

aligned with the velocity vector, the change in Jacobi value are nonzero in general. However, as observed in Figure 14(b), when the thrust magnitude falls to $f =$ 1e-14, the change in Jacobi value is zero to the same accuracy as the natural baseline solutions.

Note that the absolute and relative tolerances for the numerical integration algorithms leveraged in this comparison are 1e-14. Thus, the minimum low-thrust magnitude is comparable to the numerical error constraint in the integration. Replicating the comparison with the absolute and relative tolerances set to 1e-10 confirms this conclusion: the minimum significant low-thrust perturbation is roughly equivalent to the integration algorithm tolerance. It is additionally instructive to consider the physical characteristics of a low-thrust system with these small thrust magnitudes. For example, a thrust level of $f =$ 1e-14 in the Earth-Moon system corresponds to a 1000 kg spacecraft with a 27.3 femptonewton thrust magnitude. Thrusters capable of delivering such small forces do not yet exist, thus, any realistic low-thrust propulsion system may be modeled in the CR3BP-LT model without loss of numerical accuracy.

SUMMARY AND FUTURE WORK

To gain insights that are useful in low-thrust mission design applications, dynamical structures in the combined low-thrust multi-body dynamics are explored. The full 10-dimensional equations of motion are simplified via a series of dimension reductions, including a constant thrust formulation that preserves the circular restricted three-body problem (CR3BP) integral, the Jacobi constant. The equilibrium solutions of the low-thrust CR3BP (CR3BP-LT) are computed as a function of the low-thrust pointing direction; the locations of these solutions are similar to the natural CR3BP Lagrange points at small thrust magnitudes but librate from the natural points as the thrust magnitude increases. Both the location and stability of the CR3BP-LT equilbria are available from an analysis of the natural CR3BP dynamics.

Periodic motion exists in the CR3BP-LT model within the vicinity of the equilibrium solutions and is similar to the familiar CR3BP periodic orbits. Given the increased number of independent variables, families of periodic orbits are continued in several parameters to yield a variety of similar solutions. Finally, manifold arcs from the natural CR3BP periodic orbits are augmented with low-thrust and compared to the natural manifolds in configuration space and on Poincaré maps. The addition of low-thrust to the manifold motion bends the tube geometry in the direction of the thrust vector and enables transit between regions that are separated by natural dynamical barriers.

Many facets of this study warrant future work. For example, efforts to leverage advanced continuation algorithms in the CR3BP-LT model will yield a more complete representation of periodic motion in the combined dynamics. Similarly, many combinations of low-thrust and natural manifolds with low-thrust and natural periodic orbits remain unexplored. Finally, an investigation of motion in the P_2 region via periapse maps may supply insight to guide the design of low-thrust capture and escape itineraries, such as the Lunar IceCube mission. The application of such apse maps is particularly interesting when the thrust pointing is chosen to maximize the change in energy and may predict local optima.

ACKNOWLEDGEMENTS

This work was completed at Purdue University and at the Goddard Space Flight Center in Greenbelt, Maryland. This research is supported by a NASA Space Technology Research Fellowship, NASA Grant NNX16AM40H. The authors wish to thank the Purdue University school of Aero-

nautics and Astronautics as well as the NASA Goddard Navigation and Mission Design branch for their facilities and support. Additionally, many thanks to the Purdue Multi-Body Dynamics Research Group for interesting discussions and ideas.

REFERENCES

[1] G. Mingotti, F. Topputo, and F. Bernelli-Zazzera, "Combined Optimal Low-Thrust and Stable-Manifold Trajectories to the Earth-Moon Halo Orbits," *AIP Conference Proceedings*, AIP, 2007, 10.1063/1.2710047.

[2] J. Stuart, *A Hybrid Systems Strategy for Automated Spacecraft Tour Design and Optimization*. PhD Dissertation, Purdue University, May 2014.

[3] G. Mingotti, F. Topputo, and F. Bernelli-Zazzera, "Optimal Low-Thrust Invariant Manifold Trajectories via Attainable Sets," *Journal of Guidance, Control, and Dynamics*, Vol. 34, November 2011, pp. 1644–1656, 10.2514/1.52493.

[4] D. Grebow, M. Ozimek, and K. Howell, "Design of Optimal Low-Thrust Lunar Pole-Sitter Missions," *The Journal of the Astronautical Sciences*, Vol. 58, January-March 2011, pp. 55–79.

[5] V. Szebehely, *Theory of Orbits: The Restricted Problem of Three Bodies*. Academic Press, 1967.

[6] K. C. Howell, B. T. Barden, R. S. Wilson, and M. W. Lo, "Trajectory Design using A Dynamical Systems Approach With Application to GENESIS," *AAS/AIAA Astrodynamics Specialists Conference*, August 1997.

[7] C. Roberts, "Long Term Missions at the Sun-Earth Libration Point L1: ACE, SOHO, and WIND," *Advances in the Astronautical Sciences*, Vol. 142, No. 2, 2011, pp. 1263–1282.

[8] C. Conley, "Low Energy Transit Orbits in the Restricted Three-Body Problem," *Society for Industrial and Applied Mathematics Journal on Applied Mathematics*, Vol. 16, 1968, pp. 732–746.

[9] W. Koon, M. Lo, J. Marsden, and S. Ross, "Heteroclinic Connections Between Periodic Orbits and Resonance Transitions in Celestial Mechanics," *Chaos*, Vol. 10., 2000.

[10] G. Gómez, W. Koon, M. Lo, and J. Marsden, "Connecting Orbits and Invariant Manifolds in the Spatial Restricted Three-Body Problem," *Nonlinearity*, Vol. 17, 2004.

[11] M. Rayman, P. Varghese, D. Lehman, and L. Livesay, "Results From the Deep Space 1 Technology Validation Mission," *International Astronautical Congress, Session IAA.11.2: Small Planetary Missions. Amsterdam, The Netherlands*, 1999.

[12] H. Kuninaka, K. Nishiyama, Y. Shimizu, I. Funaki, and H. Koixumi, "Hayabusa Asteroid Explorer Powered by Ion Engines on the way to Earth," *31st International Electric Propulsion Conference*, University of Michigan, Ann Arbor, Michigan, USA, September 2009.

[13] C. Russel and C. Raymond, *The Dawn Mission to Minor Planets 4 Vesta and 1 Ceres*. Springer, 2012.

[14] N. Bosanac, A. Cox, K. Howell, and D. Folta, "Trajectory Design for a Cislunar Cubesate Leveraging Dynamical Systems Techniques: The Lunar IceCube Mission," *27th AAS/AIAA Space Flight Mechanics Meeting*, San Antonio, TX, February 2017.

[15] A. Farrés and N. Miguel, "Solar Sailing at the L4/L5 Libration Points," *AAS/AIAA Astrodynamics Specialist Conference*, Columbia River Gorge, Stevenson, WA, 2017.

[16] W. H. Press, S. A. Teukolsky, W. T. Vetterling, and B. P. Flannery, *Numerical Recipes: The Art of Scientific Computing*. New York, New York: Cambridge University Press, 3rd ed., 2007.

[17] S. Wiggins, L. Wiesenfeld, C. Jaffé, and T. Uzer, "Impenetrable Barriers in Phase-Space," *Physical Review Letters*, Vol. 86, June 2001, pp. 5478–5481, 10.1103/PhysRevLett.86.5478.

[18] C. H. Acton, "Ancillary Data Services of NASAs Navigation and Ancillary Information Facility," *Planetary and Space Science*, Vol. 44, No. 1, 1996, pp. 65–70.